Original Article

Institution of MECHANICAL ENGINEERS
Journal of MECHANICAL ENGINEERING SCIENCE

Proc IMechE Part C:
J Mechanical Engineering Science
2020, Vol. 234(1) 121–136

DOI: 10.1177/0954406219869985
journals.sagepub.com/home/pic
SAGE

Complete kinematic calibration of a 6-RRRPRR parallel kinematic machine based on the optimal measurement configurations

Chunyang Han[1,2,3], Yang Yu[1], Zhenbang Xu[1], Xiaoming Wang[1,2], Peng Yu[1] and Xiaoqin Zhou[3]

Abstract

This paper presents a kinematic calibration of a 6-RRRPRR parallel kinematic mechanism with offset RR-joints that would be applied in space positioning field. In order to ensure highly accurate and highly effective calibration process, the complete error model, which contains offset universal joint errors, is established by differentiating inverse kinematic model. A calibration simulation comparison with non-complete error model shows that offset universal joint errors are crucial to improve the calibration accuracy. Using the error model, an optimal calibration configuration selection algorithm is developed to determine the least number of measurement configurations as well as the optimal selection of these configurations from the feasible configuration set. To verify the effectiveness of kinematic calibration, a simulation and experiment were performed. The results show that the developed approach can effectively improve accuracy of a parallel kinematic mechanism with relatively low number of calibration configurations.

Keywords

Parallel kinematic machine, complete error model, observability index, optimal measurement configurations, calibration experiment

Date received: 25 January 2019; accepted: 9 July 2019

Introduction

The parallel kinematic mechanism (PKM) has been successfully used as the secondary mirror positioning machine of the large ground-based optical telescope in recent years.[1–3] However, the stiffness and accuracy are the major technique problems faced by the application of the active adjustment device to space optical loads.[4–6] In recent years, a large number of studies have shown that the design of joint used in PKM is the key component to determine its stiffness.[5,7] In related literature, R, U, S, C and *P* denote a revolute pair, a universal joint, a spherical joint, a cylindrical pair, and an actuated prismatic pair.[8] The offset design of RR-joint makes pivoting range of joint larger and also makes the parallel structure more stiffer than traditional S-joint and U-joint.[9] Gloess and Lula analyzed that the offset RR-joint is twice the load capacity of U-joint.[10] Besides, the offset RR-joint is easier to manufacture than the S-joint and U-joint due to the universal joint that is replaced by two separate revolute joints.

In this paper, a PKM with RRRPRR kinematic chain is mainly used as the secondary mirror adjustment system of a large space telescope. Compared to precise fabrication and assembly, kinematic calibration is more effective and lower cost way to improve the accuracy of parallel manipulators.[11–13] Generally, kinematic calibration of the PKM includes error modeling, pose measurements, identification of geometric errors, and error compensation.[14] By establishing the kinematic and error models as well as measuring

[1]Changchun Institute of Optics, Fine Mechanics and Physics, Chinese Academy of Sciences, Changchun, China
[2]Department of Mechanical Manufacture and Automation, University of Chinese Academy of Sciences, Beijing, China
[3]School of Mechanical and Aerospace Engineering, Jilin University, Changchun, China

Corresponding author:
Zhenbang Xu, Changchun Institute of Optics, Fine Mechanics and Physics, Chinese Academy of Sciences, No 3888 Dong Nanhu Road, Changchun 130033, China.
Email: xuzhenbang@gmail.com

the pose (position and orientation) and actuator movements of the PKM within the workspace, parameter identification equations can be established from which optimal solutions for the geometric errors can be derived.[15]

In the process of kinematic calibration, the error model has a strong relationship with the computational stability and calibration result. Compared to kinematic calibration of traditional 6-SPS, 6-UCU, and 6-UPS configurations PKMs, the offset RR-joints introduced the offset parameters of hinge axis into kinematics model, which increases the number of kinematic parameters to be identified. To simplify the difficulties of kinematic calibration and error modeling, universal (U) and spherical joints are usually regarded as points without considering other defects[16,17] such as machining error, assembly error, and joint rigidity.[18] Sun formulated the error model of a three-degrees-of-freedom (3-DOF) rotational parallel manipulator that considered all possible geometric source errors, and in order to decrease the difficulty and complexity of the kinematic calibration, sensitivity analysis of all geometric source errors based upon Monte Carlo method was carried out.[19] Kong et al.[20] investigated the influence of imperfect universal joints on increasing the positioning accuracy for a 3-DOF parallel manipulator. They found that considering the defects of the universal joints leads to a small improvement in accuracy. However, for the high-accuracy adjustment requirements of a PKM system with an offset hinge in a large space telescope,[21] the ignored kinematic parameters that cannot be identified by kinematic calibration[22,23] prevent the parallel mechanism from achieving higher levels of absolute positioning accuracy.[24]

The measurement scheme determines the effectiveness and cost of kinematic calibration work. Basically, all measurement schemes can be classified into two categories: complete and incomplete measurements. Many studies have been conducted on complete measurements with various devices.[25] However, calibration is a time-consuming process, and the high number of poses or configurations required for calibration is impractical to measure. Instead of laboriously striving for complete-measurement configuration information, most studies impose some constraints to reduce the dimensions of the calibration configuration set, such as cylinder,[26] orientation,[27,28] distance,[29] or position constraints.[30] However, incomplete measurements approach is not efficient, and corresponding measuring method would change completely when dealing with different PKMs.[31] Besides, with the reduction of measurement configuration dimension, these measurement noise caused by test fixture error and limited measurement equipment precision is propagated to the identified kinematic parameters. Therefore, the effect of measurement noise on the kinematic calibration has to be minimized.[32–34] To reach a compromise between calibration accuracy and efficiency, an optimal calibration configuration selection is the determination of complete measurement configuration for achieving the best accuracy with the optimal number and combinations of experiments. Several studies on PKM systems have been conducted to determine the optimal plan for measurement configuration. Daney et al.[35] presented an iterative one-by-one pose search algorithm to search for a given number of optimal poses within an infinite-but-bounded or a finite set of configurations. However, this study does not mention how to determine the number of optimal poses. Zhou et al.[36] indicated that determining the number of optimal measurement poses is as important as selecting the poses themselves for improving the robot calibration accuracy. Nategh and Agheli[37] employed observability indices to find the most visible measurement configurations and optimum number of configurations. This approach significantly increased the robustness of the PKM calibration with respect to measurement noise, but the optimization methods are sensitive to local minima.

In contrast to kinematic calibration of common 6-SPS, 6-UCU, and 6-UPS configurations PKMs, the inverse kinematics of a 6-RRRPRR configuration cannot be easily solved by vector methods, and the effect of offset universal joint errors on calibration accuracy needs to be considered in the proposed kinematic calibration. Therefore, a complete error model that contains the RR-joint offset defects is established to identify the global kinematic parameters. Compared with the common optimal configurations selection algorithm that only considers the number or combination of configurations in the global workspace, this paper proposes an optimal method to achieve a compromise between calibration accuracy and efficiency with the optimal number and combinations of configurations in the feasible configuration set.

In the following section, a PKM with a RRRPRR kinematic chain was introduced, and the associated kinematic models were developed. Kinematic calibration simulation was carried out in a further section. The penultimate section described how the proposed approach had been implemented on a 6-DOF secondary-mirror adjustment mechanism (SMAM). Experimental results proved that the proposed PKM calibration method was very effective and accurate. The last section concluded this study.

Structural modeling

A PKM is composed of a base platform connected to a mobile platform with six kinematic chains (as shown in Figure 1(a)). Each RRRPRR kinematic chain, which has two RR-joints and one ball screw unit without guide mechanisms (as shown in Figure 1(b)), is described below. The reference system $O_B - X_B Y_B Z_B$ and mobile system $O_P - X_P Y_P Z_P$ are fixed at

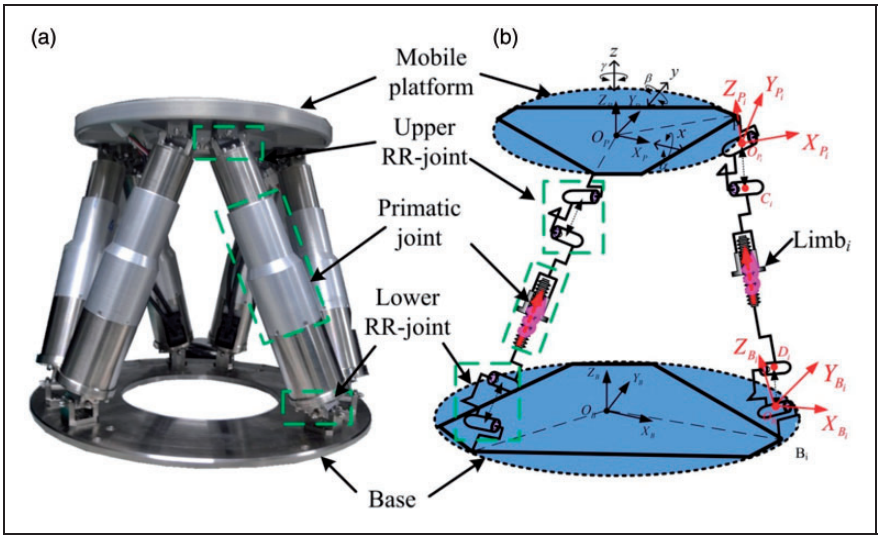

Figure 1. (a) 6RRRPRR PKM and (b) schematic diagram of the *i*-th actuator.

the center of base and mobile platform. The connecting line of six upper hinge point P_i ($I=1$–6) on the mobile platform and six lower hinge point B_i ($I=1$–6) on the base forms a hexagon with a symmetrical distribution of 120°, respectively. Because of the existence of RR-joint, two inclination angle variables are added to each limb. Therefore, the local coordinate system $O_{B_i}-X_{B_i}Y_{B_i}Z_{B_i}$ $(I=1,\ldots,6)$ is established based on the lower hinge point $B_i(I=1$–$6)$, and X_{B_i}-axis direction is from point O_B to point B_i. The second local coordinate system $O_{P_i}-X_{P_i}Y_{P_i}Z_{P_i}$ $(I=1,\ldots,6)$ is established based on the upper hinge point P_i ($I=1$–6), and X_{P_i}-axis direction is from point O_P to point P_i.

Inverse kinematics modeling

The inverse kinematic solution is to solve for the driving distance of the actuator when the pose $\boldsymbol{p}$ of the moving platform relative to the base is given. In reference system $O_B-X_BY_BZ_B$, point D_i represents another rotating center of the lower offset joint adjacent to B_i, and point C_i represents another rotating center of the upper offset joint adjacent to P_i, the *i*-th limb between point C_i and D_i is derived as below

$$\boldsymbol{L}_i = {}^{O_B}\overline{C_iD_i} = {}^{O_B}_{O_P}\mathbf{T}\cdot{}^{O_P}_{O_{P_i}}\mathbf{T}\cdot{}^{P_i}\overline{P_iC_i} - {}^{O_B}_{O_{B_i}}\mathbf{T}\cdot{}^{B_i}\overline{B_iD_i} \tag{1}$$

where matrix ${}^{Y}_{X}\mathbf{T}$ represents the transformation matrix from frame X to frame Y.

Complete error model

Kinematic parameter errors that include manufacturing tolerance and clearances, joint installation error and actuator control error can cause error in the pose of the PKM. A schematic description of the *i*-th kinematic chain of the PKM is shown in Figure 2(a), where length L_i is the distance between points C_i and D_i. Vector u_i can be expressed as the unit vector. Variable ψ_{B_i} is the angle between Y_{B_i}-axis and line B_iC_i. Moreover, variable ψ_{P_i} is the angle between the Y_{P_i}-axis and line P_iD_i. Variable φ_{bi} is the angle between X_{B_i}-axis and X_B-axis, and variable φ_{pi} is the angle between the X_{P_i}-axis and X_P-axis. Offset distance L_{Pi} is the vertical distance between upper hinge point P_i and point D_i, and L_{Bi} is the vertical distance between lower hinge point B_i and point C_i.

An error diagram that describes the *i*-th kinematic parameter error chain contribution to the pose error of the platform is displayed in Figure 2(b). The circles indicate the error boundaries about the nominal points, dotted lines indicate nominally closed loops, and solid lines indicate actual closed loops due to kinematic errors. A differential error model is obtained by differentiating equation (1) as follows

$$\begin{aligned}\delta\boldsymbol{L}_i\boldsymbol{u}_i + \boldsymbol{L}_i\delta\boldsymbol{u}_i = {}&\delta\left({}^{O_B}_{O_P}\boldsymbol{x}\right) + \left(\delta({}^{O_B}_{O_P}\boldsymbol{\theta})\times{}^{O_B}_{O_P}\mathbf{R}\right)\cdot\\ &\left({}^{O_P}_{O_{P_i}}\mathbf{R}^{P_i}\boldsymbol{C}_i + {}^{O_P}_{O_{P_i}}\boldsymbol{x}_i\right) + \cdots\\ &+ {}^{O_B}_{O_P}\mathbf{R}\delta^{O_P}_{O_{P_i}}\boldsymbol{x}_i - \delta^{O_B}_{O_{B_i}}\boldsymbol{x}_i + \cdots\\ &+ {}^{O_B}_{O_P}\mathbf{R}^{O_P}_{O_{P_i}}\mathbf{R}\delta^{O_{P_i}}\boldsymbol{C}_i - {}^{O_B}_{O_{B_i}}\mathbf{R}\delta^{O_{B_i}}\boldsymbol{D}_i\end{aligned} \tag{2}$$

where ${}^{O_B}_{O_P}\boldsymbol{x} = [x \quad y \quad z]$ and ${}^{O_B}_{O_P}\boldsymbol{\theta} = [\alpha \quad \beta\gamma]$ are the position and orientation vectors of the top center position, respectively;

$${}^{O_B}_{O_P}\mathbf{R} = \begin{bmatrix} c\gamma c\beta & c\gamma s\beta s\alpha - s\gamma c\alpha & c\gamma s\beta c\alpha + s\alpha s\gamma \\ s\gamma c\beta & s\gamma s\beta s\alpha + c\gamma c\alpha & s\gamma s\beta c\alpha - c\gamma s\alpha \\ -s\beta & c\beta s\alpha & c\beta c\alpha \end{bmatrix}$$

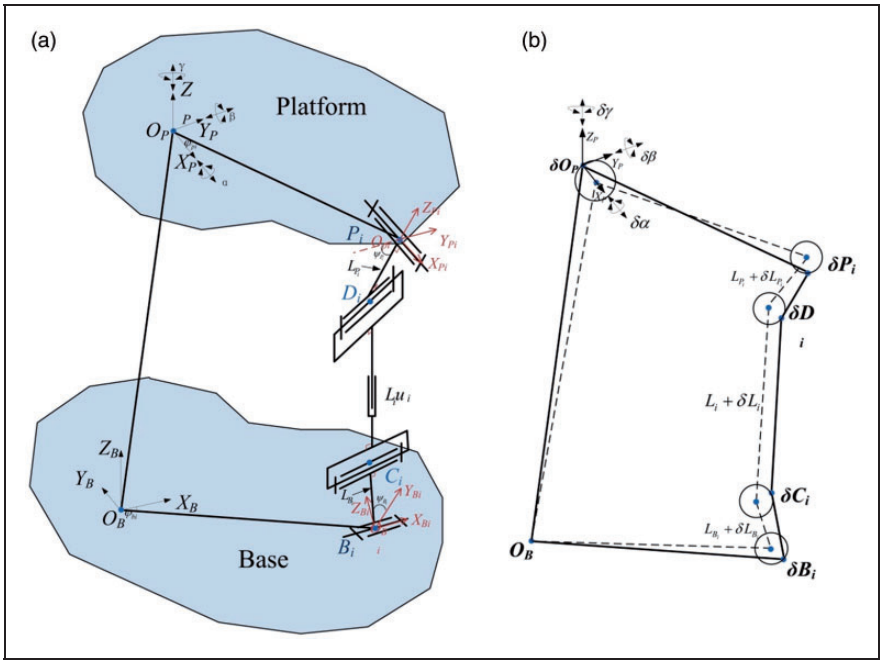

Figure 2. (a) Schematic diagram of the *i*-th chain and (b) error diagram.

represents global rotation matrix from frame $O_P - X_P Y_P Z_P$ to frame $O_B - X_B Y_B Z_B$;

$$ {}^{O_B}_{O_{B_i}}\mathbf{R} = \begin{bmatrix} c\varphi_{bi} & -s\varphi_{bi} & 0 \\ s\varphi_{bi} & c\varphi_{bi} & 0 \\ 0 & 0 & 1 \end{bmatrix} $$

represents local rotation matrix from the *i*-th frame $O_{B_i} - X_{B_i} Y_{B_i} Z_{B_i}$ to frame $O_B - X_B Y_B Z_B$;

${}^{O_B}_{O_{B_i}}\boldsymbol{x_i}$ is the position vectors from the *i*-th frame $O_{B_i} - X_{B_i} Y_{B_i} Z_{B_i}$ to frame $O_B - X_B Y_B Z_B$;

$$ {}^{O_P}_{O_{P_i}}\mathbf{R} = \begin{bmatrix} c\varphi_{pi} & -s\varphi_{pi} & 0 \\ s\varphi_{pi} & c\varphi_{pi} & 0 \\ 0 & 0 & 1 \end{bmatrix} $$

represents local rotation matrix from the *i*-th frame $O_{P_i} - X_{P_i} Y_{P_i} Z_{P_i}$ to frame $O_P - X_P Y_P Z_P$;

${}^{O_P}_{O_{P_i}}\boldsymbol{x_i}$ is the position vectors from the *i*-th frame $O_{P_i} - X_{P_i} Y_{P_i} Z_{P_i}$ to frame $O_P - X_P Y_P Z_P$;

${}^{O_{P_i}}\boldsymbol{D_i} = \begin{bmatrix} 0 & \mathrm{L}_{p_i} \cdot c\psi_{p_i} & \mathrm{L}_{p_i} \cdot c\psi_{p_i} \end{bmatrix}^T$ is vector in frame $O_{P_i} - X_{P_i} Y_{P_i} Z_{P_i}$;

${}^{O_{B_i}}\boldsymbol{C_i} = \begin{bmatrix} 0 & L_{b_i} \cdot c\psi_{b_i} & L_{b_i} \cdot c\psi_{b_i} \end{bmatrix}^T$ is vector in frame $O_{B_i} - X_{B_i} Y_{B_i} Z_{B_i}$, and $s(\cdot) = \sin(\cdot)$, $c(\cdot) = \cos(\cdot)$.

It is assuming that the unit direction vector $\boldsymbol{u_i}$ is almost parallel to that in the nominal kinematic model. Hence, δu_i is zero, equation (2) is applied to the six limbs of the PKM, and the complete error model in matrix form can be obtained as follows

$$ \mathbf{J}_1 \delta\widehat{\boldsymbol{D}} = \mathbf{E}\delta\boldsymbol{L} + \mathbf{N}_1\delta\boldsymbol{P} + \mathbf{N}_2\delta\boldsymbol{B} + \mathbf{M}_1\delta\boldsymbol{L}_B + \mathbf{M}_2\delta\boldsymbol{L}_P \tag{3} $$

where $\delta\boldsymbol{L} = [\delta L_1 \quad \delta L_2 \quad \delta L_3 \quad \delta L_4 \quad \delta L_5 \quad \delta L_6]^T$ is the length error vector of the limbs, which includes the actuator error and the structure error; $\mathbf{E} \in \mathbf{R}^{6\times6}$ is the unit matrix.

$$ \mathbf{J}_1 = \begin{bmatrix} \boldsymbol{u}_1^T & \left({}^{O_B}_{O_P}\mathbf{R} \cdot \left({}^{O_P}_{O_{P_1}}\mathbf{R}^{P_1} C_1 + {}^{O_P}_{O_{P_1}} X_1\right)\right) \times \boldsymbol{u}_1^T \\ \vdots & \vdots \\ \boldsymbol{u}_6^T & \left({}^{O_B}_{O_P}\mathbf{R} \cdot \left({}^{O_P}_{O_{P_6}}\mathbf{R}^{P_6} C_6 + {}^{O_P}_{O_{P_6}} X_6\right)\right) \times \boldsymbol{u}_6^T \end{bmatrix} \in \mathbf{R}^{6\times6} $$

is the pose error transfer matrix;

$$ \delta\widehat{\boldsymbol{D}} = \begin{bmatrix} \delta\left({}^{O_B}_{O_P}\boldsymbol{X}\right) \\ \delta\left({}^{O_B}_{O_P}\boldsymbol{\theta}\right) \end{bmatrix} \in R^{6\times1} $$

is the platform pose error; vector,

$$ \delta\boldsymbol{B} = \begin{bmatrix} \delta^{O_B}_{O_{B_1}} X_1 \\ \vdots \\ \delta^{O_B}_{O_{B_6}} X_6 \end{bmatrix} \in R^{18\times1} $$

and $\delta\boldsymbol{P} = \begin{bmatrix} \delta^{O_P}_{O_{P_1}} X_1 \\ \vdots \\ \delta^{O_P}_{O_{P_6}} X_6 \end{bmatrix} \in R^{18\times1}$ are joint installation error; vectors, $\delta\boldsymbol{L}_B = \begin{bmatrix} \delta L_{B_1} \\ \vdots \\ \delta L_{B_6} \end{bmatrix} \in R^{6\times1}$ and

$\delta \boldsymbol{L}_P = \begin{bmatrix} \delta L_{P_1} \\ \vdots \\ \delta L_{P_6} \end{bmatrix} \in R^{6\times 1}$ are the offset error vectors of the RR-joint; and

$$\mathbf{N}_1 = \begin{bmatrix} -\boldsymbol{u}_1{}^T {}^{O_B}_{O_P}\mathbf{R} & \cdots & 0 \\ \vdots & \ddots & \vdots \\ 0 & \cdots & -\boldsymbol{u}_6{}^T {}^{O_B}_{O_P}\mathbf{R} \end{bmatrix} \in \mathbf{R}^{6\times 18},$$

$$\mathbf{M}_1 = \begin{bmatrix} \boldsymbol{u}_1{}^T {}^{O_B}_{O_{B_1}}\mathbf{R}^{O_{B_1}}\boldsymbol{u}_1 & \cdots & 0 \\ \vdots & \ddots & \vdots \\ 0 & \cdots & \boldsymbol{u}_6{}^T {}^{O_B}_{O_{B_6}}\mathbf{R}^{O_{B_6}}\boldsymbol{u}_6 \end{bmatrix} \in \mathbf{R}^{6\times 6}$$

$$\mathbf{N}_2 = \begin{bmatrix} \boldsymbol{u}_1{}^T & \cdots & 0 \\ \vdots & \ddots & \vdots \\ 0 & \cdots & \boldsymbol{u}_6{}^T \end{bmatrix} \in \mathbf{R}^{6\times 18}$$

and

$$\mathbf{M}_2 = \begin{bmatrix} -\boldsymbol{u}_1^T {}^{O_B}_{O_P}\mathbf{R}^{O_P}_{O_{P_1}}\mathbf{R}^{O_{P_1}}\boldsymbol{u}_1 & \cdots & 0 \\ \vdots & \ddots & \vdots \\ 0 & \cdots & -\boldsymbol{u}_6^T {}^{O_B}_{O_P}\mathbf{R}^{O_P}_{O_{P_6}}\mathbf{R}^{O_{P_6}}\boldsymbol{u}_6 \end{bmatrix} \in \mathbf{R}^{6\times 6}$$

are the diagonal matrices that imply geometrically how the non-actuation errors (RR-joint offset defects and RR-joint installation) are mapped to the actuator errors.

For the purpose of kinematic calibration, m measurement configurations are selected. The PKM error model that is derived from equation (3) is given as

$$^{\mathrm{m}}\delta\widehat{D} = {}^{m}\mathbf{J}\delta\widehat{\rho} \tag{4}$$

where $^{m}\delta\widehat{\boldsymbol{D}} = {}^{m}\begin{bmatrix} \delta\left({}^{O_B}_{O_P}\boldsymbol{X}\right) \\ \delta({}^{O_B}_{O_P}\boldsymbol{\theta}) \end{bmatrix} \in R^{6m\times 1}$ denotes the m configurations errors; $^{m}\mathbf{J} = {}^{m}\mathbf{J}_1{}^{-1}\left[{}^{m}\mathbf{E} \quad {}^{m}\mathbf{N}_1 \quad {}^{m}\mathbf{N}_2 \quad {}^{m}\mathbf{M}_1 \quad {}^{m}\mathbf{M}_2\right] \in \mathbf{R}^{6m\times 54}$ is the Jacobian matrix including the m measurement configurations; and $\delta\widehat{\boldsymbol{\rho}} = \left[\delta\boldsymbol{L} \quad \delta\boldsymbol{P} \quad \delta\boldsymbol{B} \quad \delta\boldsymbol{L}_B \quad \delta\boldsymbol{L}_P\right]^T \in R^{54\times 1}$ is the error vector, which includes the 54 kinematic parameters.

Cost function

The kinematic calibration of the 6RRRPRR PKM involves 54 structure parameters identification. It uses the residuals between the theoretical value of the actuator input and the measured value which is calculated using the inverse kinematic model and actual pose to construct the identification equation.[37] The cost function, defined for some measurement configurations, is given as

$$CF = \sum_{j=1}^{m}\sum_{i=1}^{6}\left[\left\|{}^{O_B}_{O_P}\mathbf{T}\cdot{}^{O_P}_{O_{P_i}}\mathbf{T}\cdot{}^{P_i}\overline{P_iC_i} - {}^{O_B}_{O_{B_i}}\mathbf{T}\cdot{}^{B_i}\overline{B_iD_i}\right\|^2 - \left(\boldsymbol{L}_{i,j}\right)^2\right]^2 \tag{5}$$

where $\left\|{}^{O_B}_{O_P}\mathbf{T}\cdot{}^{O_P}_{O_{P_i}}\mathbf{T}\cdot{}^{P_i}\overline{P_iC_i} - {}^{O_B}_{O_{B_i}}\mathbf{T}\cdot{}^{B_i}\overline{B_iD_i}\right\|^2$ is the norm of the limb length derived from the inverse kinematic at the actual pose j; and $L_{i,j} = \overline{L}_{oi} + \Delta L_{i,j}$ is the i-th length which is a sum of the initial leg $\overline{L}_{oi}$ and the length variation $\Delta L_{i,j}$ at nominal pose j. The least squares approach based on the Levenberg–Marquardt algorithm is used to minimize the cost function.

Kinematic calibration simulation

Structural parameter identification

In this section, structure parameter identification is carried out by minimizing the cost function. The η represents nominal parameters. For the purpose of simulation, random errors in the range of $-1\,\mathrm{mm} \leqslant \text{error} \leqslant 1\,\mathrm{mm}$ are added to the nominal parameters to obtain simulated actual parameters η_1. The identification procedure consists of the following steps:

1. Nominal parameters η and simulated actual parameters η_1 of the PKM are given (as listed in Tables 1 and 2);
2. Choosing the m nominal poses of the moving platform, as shown in Table 3. The moving platform must be within the workspace;
3. Using nominal parameters η and m nominal poses, the nominal limbs are obtained in the inverse kinematics;
4. Using simulated actual parameters η_1 and m nominal limbs, the m actual poses (denoted as $\boldsymbol{p}^m$) are calculated in the forward kinematics;
5. Assuming the 54 unknown structure parameters and m actual poses $\boldsymbol{p}^m$, the m groups limb functions are acquired in the inverse kinematics;
6. Establishing the cost function Σ of kinematic calibration and using the Levenberg–Marquardt algorithm to minimize this cost function, the known structure parameters η' is updated by identifying structure parameter error $\Delta\eta$;
7. If structure parameter error $\Delta\eta < \varepsilon$, the parameters of kinematic model is modified into the controller, else go back to the step (5). The above identification procedure is outlined in Figure 3.

Table 1. Nominal parameters η of the PKM (units: mm).

I	1	2	3	4	5	6
X_{Bi}	173.867	−46.587	−127.279	−127.279	−46.587	173.867
Y_{Bi}	46.587	173.867	127.279	−127.279	−173.867	−46.587
Z_{Bi}	0.000	0.000	0.000	0.000	0.000	0.000
X_{Pi}	84.852	31.058	−115.911	−115.911	31.058	84.853
Y_{Pi}	84.852	115.911	31.058	−31.058	−115.911	−84.853
Z_{Pi}	0.000	0.000	0.000	0.000	0.000	0.000
L_{Bi}	5.000	5.000	5.000	5.000	5.000	5.000
L_{Pi}	5.000	5.000	5.000	5.000	5.000	5.000
L_i	230.715	230.715	230.715	230.715	230.715	230.715

Table 2. Actual parameters η_I of the PKM (units: mm).

I	1	2	3	4	5	6
X_{Bi}	173.961	−46.995	−126.790	−127.901	−46.214	173.234
Y_{Bi}	46.324	174.118	127.840	−128.117	−173.008	−46.036
Z_{Bi}	−0.026	−0.128	−0.106	−0.387	0.017	0.022
X_{Pi}	85.488	31.648	−115.622	−116.154	31.681	84.918
Y_{Pi}	84.554	116.789	31.810	−30.958	−115.666	−84.679
Z_{Pi}	−0.585	−0.398	−0.058	−0.539	0.689	−0.610
L_{Bi}	5.040	5.033	5.008	5.040	5.033	4.936
L_{Pi}	4.926	5.100	4.934	4.907	5.012	5.076
L_i	230.441	230.381	230.443	230.651	230.526	231.138

Table 3. Workspace and limb stroke of the 6RRRPRR PKM.

Axis	Min (mm or deg)	Max (mm or deg)
X translation	–25	25
Y translation	–25	25
Z translation	200	240
X rotation	–15	15
Y rotation	–15	15
Z rotation	−20	20
Limb stroke	195	265

To verify the efficiency of the kinematic calibration, nine poses were randomly selected in the workspace of the PKM. For a threshold ε of 1e-7, the identification algorithm was observed to converge after six iterations. The identification results of the 54 structure parameter errors are shown in Figure 4(a). The *X*-axis represents the structure parameter classification: it displays the construction of the limb length error, upper joint position error, lower joint position error, and RR-joint offset distance error. Figure 4(a) shows that the identification results are in good agreement with the nominal parameter errors.

During the calibration experiment, the segment enclosed by red dots in Figure 3 needs to be measured using configuration measurement equipment (such as a laser tracker (LT)). To verify the robustness of the kinematic calibration, random measurement noise in the range of $-0.02\,\text{mm} \leqslant \text{error} \leqslant 0.02\,\text{mm}$ for position and $-0.004^\circ \leqslant \text{error} \leqslant 0.004^\circ$ for orientation are also taken into consideration to obtain the actual configurations. Figure 4(b) shows that the calibration results using the 29 random measurement configurations with the measurement noise in the workspace are very different from the given structure parameter errors: the maximum deviation is about 1.1 mm. As an increasing number of measurement configurations in the workspace are selected, the maximum deviation is reduced. The calibration results using 256 random measurement configurations with the measurement noise are close to the given structure parameter errors: the maximum deviation is reduced to almost 15 μm.

Verification of complete error model

In order to verify the effect of error model on kinematic calibration, the complete error model and non-complete error model that neglects RR-joint offset distance error are applied to kinematic calibration of the 6-RRRPRR PKM, respectively. Nine nominal poses are randomly selected in the workspace of the moving platform, and the nominal length is calculated by the inverse kinematics with updated structure

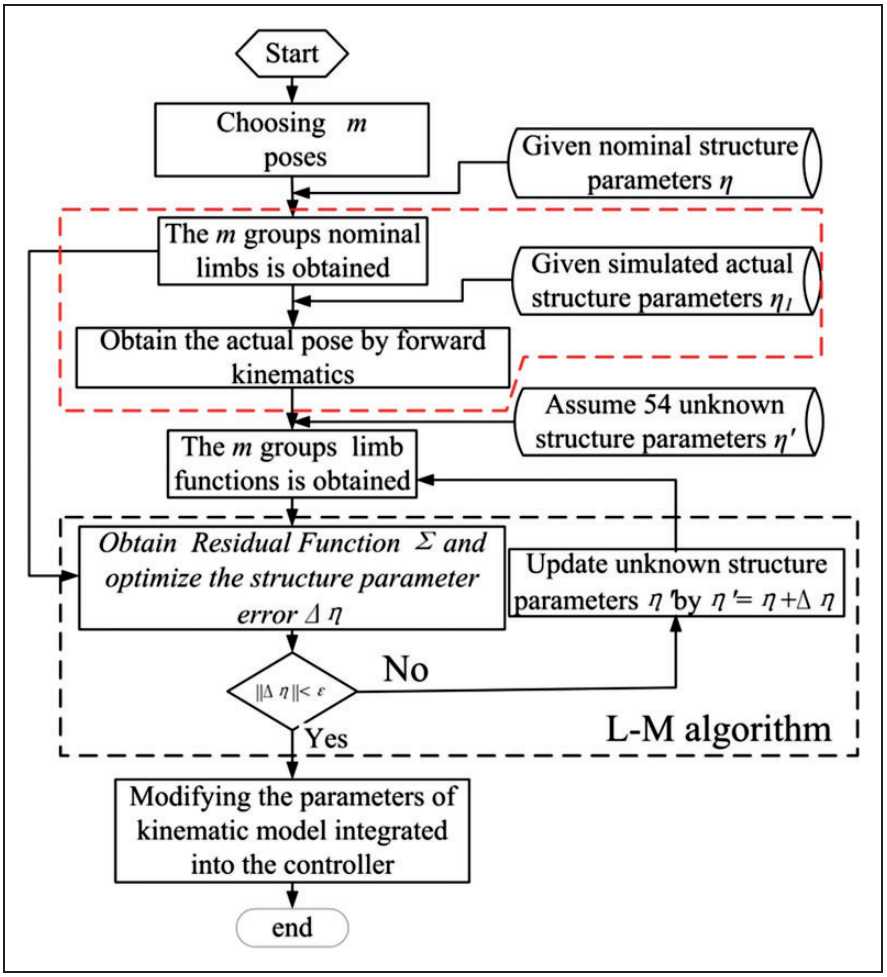

Figure 3. Kinematic calibration flowchart of a PKM.

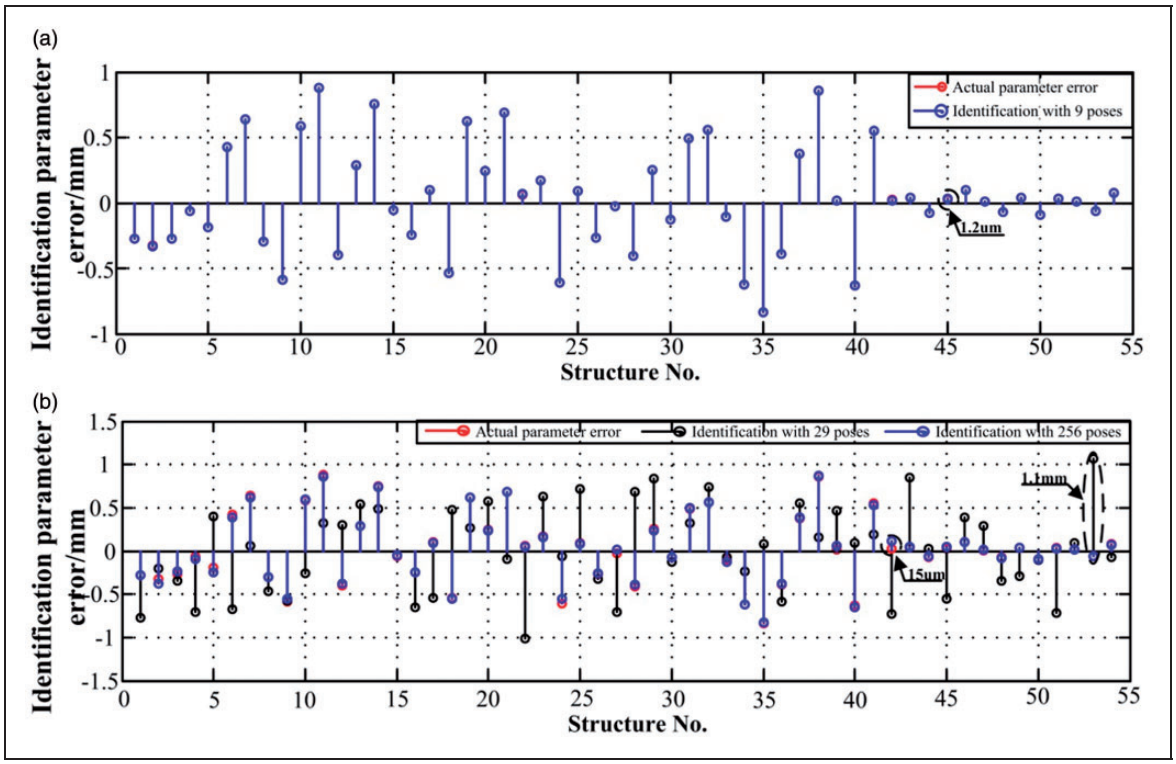

Figure 4. Results of structure parameter error identification.

parameters. Combining with the forward kinematics of actual parameters, nine actual poses are calculated, respectively.

The maximum position errors between the actual and nominal poses in the translation are shown in Figure 5, and the maximum attitude angle errors between the actual and nominal poses in the rotation are shown in Figure 6, where the X-axis represents the selected poses, and the Y-axis represents the position deviation and the attitude angle deviation. It is also found that kinematic calibration that neglects RR-joint offset distance error only makes pose accuracy at the resolution micrometer and arc second levels. An enormous improvement is achieved in the kinematic calibration when complete error model is employed.

Evaluation of the optimal calibration configuration set

To reduce the influence of external measurement noise on the kinematic calibration, the selected calibration configuration should extend through all reachable DOF as much as possible. Moreover, to increase the homogenization of the calibration results, a sufficient number of measurement configurations is regarded as beneficial.[38] However, it is impracticable to take a set of measurements that comprehensively cover the entire workspace. The optimal measurement configurations hence need to be determined.

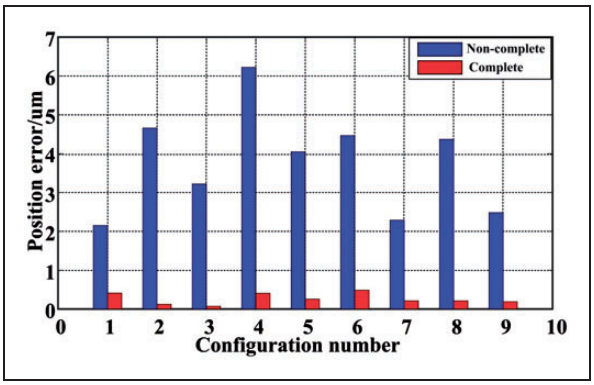

Figure 5. The position accuracy of non-complete and complete error model.

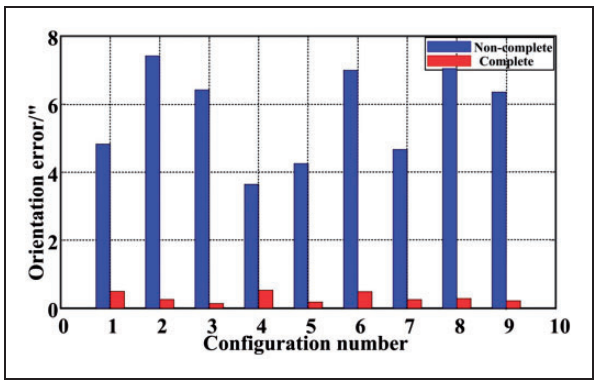

Figure 6. The orientation accuracy of non-complete and complete error model.

Feasible configuration set

To overcome the problem of local convergence and improve the efficiency of the optimal configuration selection algorithm, the optimal configuration was determined from a finite calibration configuration set (called the feasible configuration set). The Jacobian condition number is often used as an index to describe the accuracy/dexterity of the PKM.[39] A top center pose of the moving platform with a large Jacobian condition number should be selected as a feasible configuration.

As shown in equation (4), the Jacobian matrix ${}^{m}\mathbf{J}$ is determined by the pose of the moving platform. The workspace and limb strokes are listed in Table 3, and the initial height of the moving platform is 220 mm. To evaluate the influence of position on the Jacobian condition number, it is necessary to move the platform to the initial orientation angle. The Jacobian condition number nephogram is shown in Figure 7,where T_x and T_y represent translation motion along X- and Y-axis, respectively, and T_z represents five points with the same distance from the initial height to the maximum value along Z-axis. It is obvious from Figure 7 that when Z-axis translation T_z is a fixed value, a larger Jacobian condition number is generated at the points where the positive and negative boundaries of X-axis intersect the positive and negative boundaries of Y-axis, respectively. When X- and Y-axis translations are constant, the Jacobian condition number increases and the peak occurs at the highest value along Z-axis.

To evaluate the influence of orientation on the Jacobian condition number, it is necessary to move the moving platform to the initial position. The Jacobian condition number nephogram is shown in Figure 8, where R_x and R_y represent the rotation

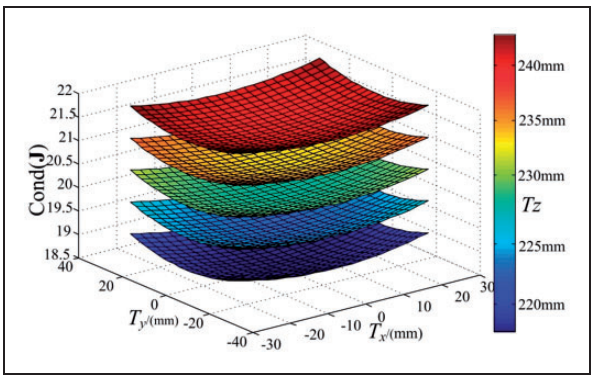

Figure 7. Jacobian condition number with respect to position.

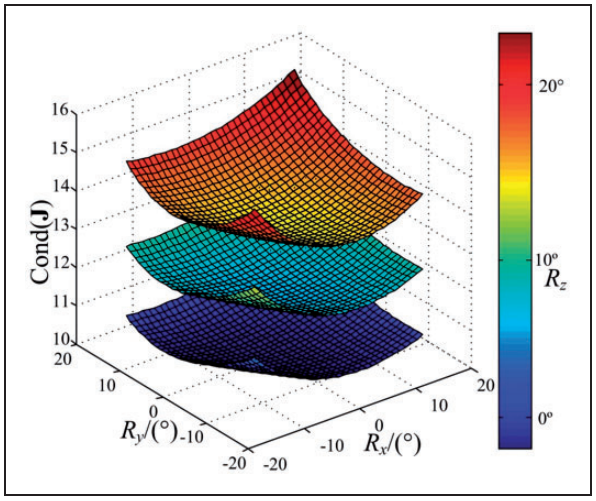

Figure 8. Jacobian condition number with respect to orientation.

along X- and Y-axis, respectively, and R_z represents three values with the same angle from zero to maximum around Z-axis. It is obvious from Figure 8 that when Z-axis rotation R_z is fixed, a larger Jacobian condition number is generated at the angles where the positive and negative boundaries of X-axis intersect the positive and negative boundaries of Y-axis, respectively. When X-axis and Y-axis rotations are constant, the Jacobian condition number increases and the peak occurs at the highest value around Z-axis.

The above analysis shows that the feasible calibration configuration set of the PKM is at the boundaries of the workspace. Two boundary poses of the six DOF can be selected. Thus, the feasible configuration set comprises the $64(2^6)$ boundary poses of the moving platform.

Optimization criteria

To evaluate the goodness of the measurement configuration, Borm–Meng and Driels-Pathre proposed the observability indexes.[40,41] It is assumed that $\delta(\Delta\widehat{\boldsymbol{\rho}})$ is the perturbation of the kinematic parameter error $\delta\widehat{\boldsymbol{\rho}}$, and ${}^m\delta(\Delta\widehat{\boldsymbol{D}})$ is the perturbation of the m configuration errors ${}^m\delta\widehat{\boldsymbol{D}}$. According to equation (4), the goodness obeys the inequality

$$\frac{\left\|\delta\left(\Delta\widehat{\boldsymbol{\rho}}\right)\right\|}{\left\|\delta\widehat{\boldsymbol{\rho}}\right\|} \leqslant \|{}^m\mathbf{J}\|\left\|{}^m\mathbf{J}^{-1}\right\| \frac{\left\|{}^m\delta\left(\Delta\widehat{\boldsymbol{D}}\right)\right\|}{\left\|{}^m\delta\widehat{\boldsymbol{D}}\right\|} \tag{6}$$

where $\|{}^m\mathbf{J}\|\left\|{}^m\mathbf{J}^{-1}\right\|$ is the amplification factor of ${}^m\delta(\Delta\widehat{\boldsymbol{D}})$ relative to $\delta(\Delta\widehat{\boldsymbol{\rho}})$. This amplification factor has a minimal value equal to one. Minimizing this factor permits us to ensure that perturbation $\delta(\Delta\widehat{\boldsymbol{\rho}})$ is "homogenized" when identifying the kinematic parameter errors. Therefore, observability index $\boldsymbol{O}({}^m\mathbf{J})$ was defined as follows[42]

$$\boldsymbol{O}({}^m\mathbf{J}) = \|{}^m\mathbf{J}\|\left\|{}^m\mathbf{J}^{-1}\right\| \tag{7}$$

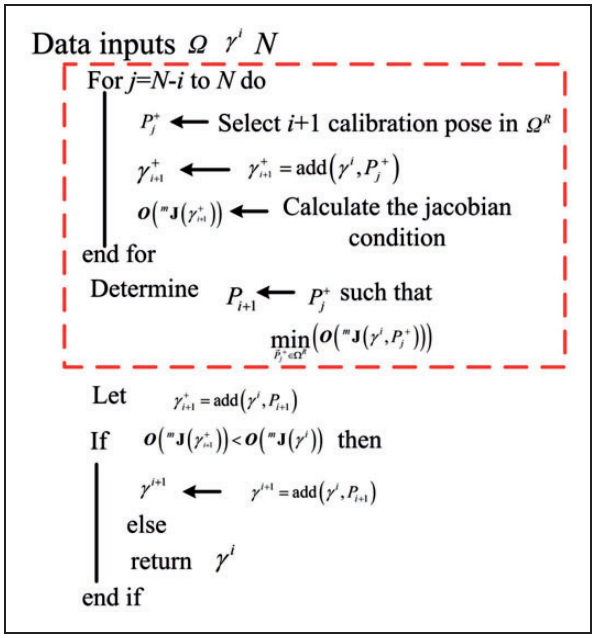

Figure 9. Algorithm for selecting the optimal measurement configuration.

Algorithm for optimal measurement configuration selection

To ensure calibration accuracy, improve measurement efficiency, and reduce measurement cost, an optimal measurement configuration selection algorithm that includes the optimal number and combinations of measurement configurations was proposed. It is supposed that Ω is the N-dimensional feasible configuration set (i.e. $N = 64$), and $\boldsymbol{P_i}$ is the i-th measurement configuration of Ω. Moreover, $\gamma^i = [P_1 \ \cdots \ P_i]$ which includes the i measurement configurations is the initial measurement configuration set. Set Ω^R which is equal to $\Omega - \gamma^i$ and consists of the $N-i$ feasible configuration set is a subset of Ω. Configuration P_j^+ is a configuration randomly chosen from Ω^R, and $\gamma_{i+1}^+ = \text{add}(\gamma^i, P_j^+)$ is obtained by adding P_j^+ to γ^i. In addition, $\gamma^{i+1} = \text{add}(\gamma^i, P_{i+1})$ which includes the i+1-th measurement configuration is the $i+1$-th optimal measurement configuration added to set γ^i, and $\boldsymbol{O}({}^m\boldsymbol{J}(\gamma^i))$ is the observability index associated with the i measurement configurations.

Initially, γ^i is randomly selected inside Ω. Then, it uses a one-by-one comparison method that is indicated by the red dotted line in Figure 9 to add the $i+1$-th calibration pose to the previous configuration set γ^i from the remaining measurement configuration set Ω^R. Observability indices $O({}^m\mathbf{J}(\gamma_{i+1}^+))$ and $O({}^m\mathbf{J}(\gamma^i))$ are compared to determine whether γ^i has

been updated. By iterating the above optimal selection process, the m optimal calibration configurations are determined. A detailed description of this process is given in Figure 9.

To determine the optimal measurement configurations, nine of the 64 feasible configuration set are first randomly selected. The 10-th optimal measurement configuration is determined and then added to the set γ^9 according to the selection algorithm in Figure 9. The above process is repeated until the observability index approaches a stable value. Thirty optimal selection procedures about the random measurement configuration set γ^9 were performed. To avoid ambiguity, the five representative optimal selection results are shown in Figure 10.

As is evident from Figure 10, each optimal selection procedure converges to a certain standard value. To further observe the variation behavior of the optimal selection procedure, the observability index for 13–44 configurations is amplified by a factor of 100. Using the optimal measurement configuration selection algorithm (Figure 9), the 10-th pose was added to the initial configuration set, and the observability index of each optimal selection procedure decreased from 10 to 27 calibration poses. Finally, each optimal selection procedure stabilized as the number of the calibration configurations increased. Note that the fourth selection procedure converges to the minimum observability index value for a measurement configuration set of 29 or more poses. Therefore, a measurement configuration set that includes 29 poses is considered to be an optimal measurement configuration for kinematic calibration.

Optimization verification

To illustrate the efficiency of the optimal measurement configurations, the results of the identification error in the structure parameter based on the 256 randomly selected measurement configurations and 29 optimal measurement configurations in the feasible pose set are shown in Figure 11. The X-axis represents the structure parameter number. The Y-axis represents the actual structure parameter errors,

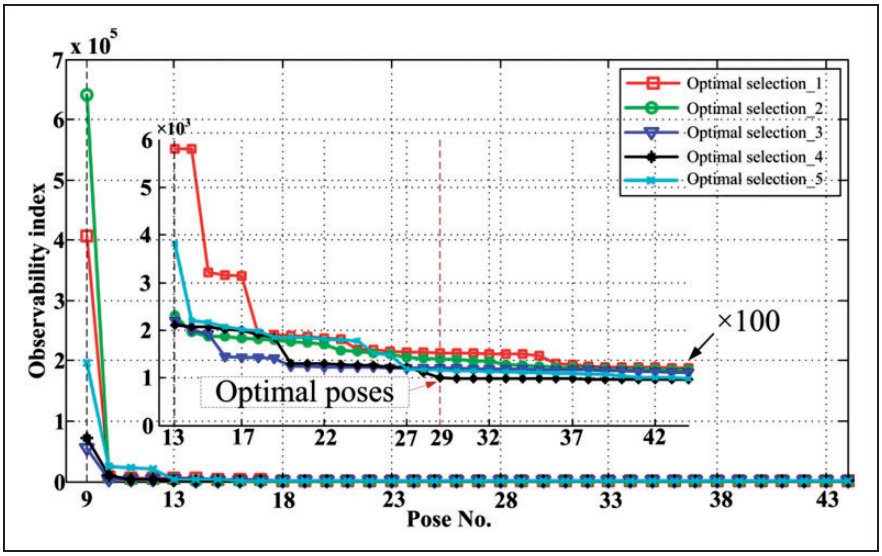

Figure 10. Observability index of the calibration configuration set.

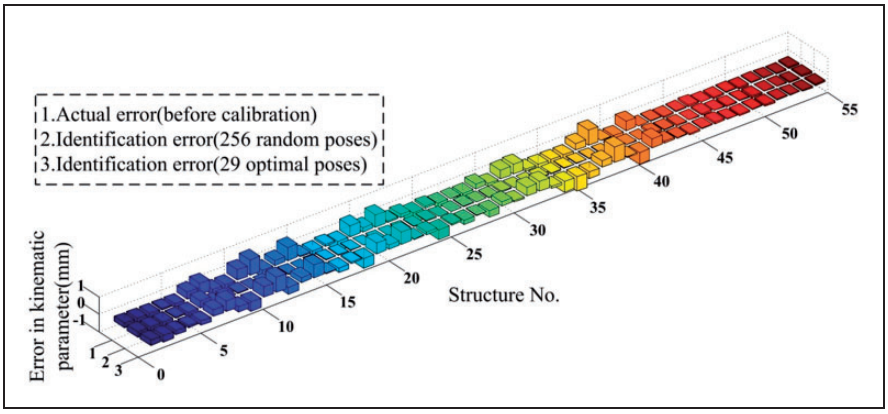

Figure 11. Errors of the kinematic parameters.

identification structure parameter errors for the 256 random poses, and identification structure parameter errors for the 29 optimal poses. It is evident that an enormous improvement is achieved in the kinematic calibration when the optimal measurement configuration is employed.

To further evaluate the performance of the optimal measurement configuration, the peak value and standard deviation of the position and orientation of 29 calibration configurations were measured in the structure parameter errors before calibration, after 256 random calibration configurations, and after 29 optimal calibration configurations. The results are listed in Table 4. This table shows that the accuracy in the position and orientation of the moving platform is clearly improved.

Calibration experiment

Experiment setup. In this section, a calibration experiment was performed on a PKM developed for the SMAM. Considering the adjustment accuracy of the SMAM, a Leica-AT901-LR LT is used to measure the positions of the spherical mounted retroreflectors (SMRs) which are placed on the reflector holders with the accuracy of 10 um + 5 um/m within the workspace 2.5 m × 5 m × 10 m. The experimental setup is shown in Figure 12.

Table 4. Statistical values for the 29 calibration configurations.

Error description / Calibration state	Position error (mm)		Orientation error (°)	
	Peak value	Std	Peak value	Std
Before calibration	0.1496	0.0673	–0.0247	0.0099
After calibration-256 random poses	0.0280	0.010	0.0069	0.0044
After calibration-29 optimal poses	0.0212	0.0089	0.0047	0.0035

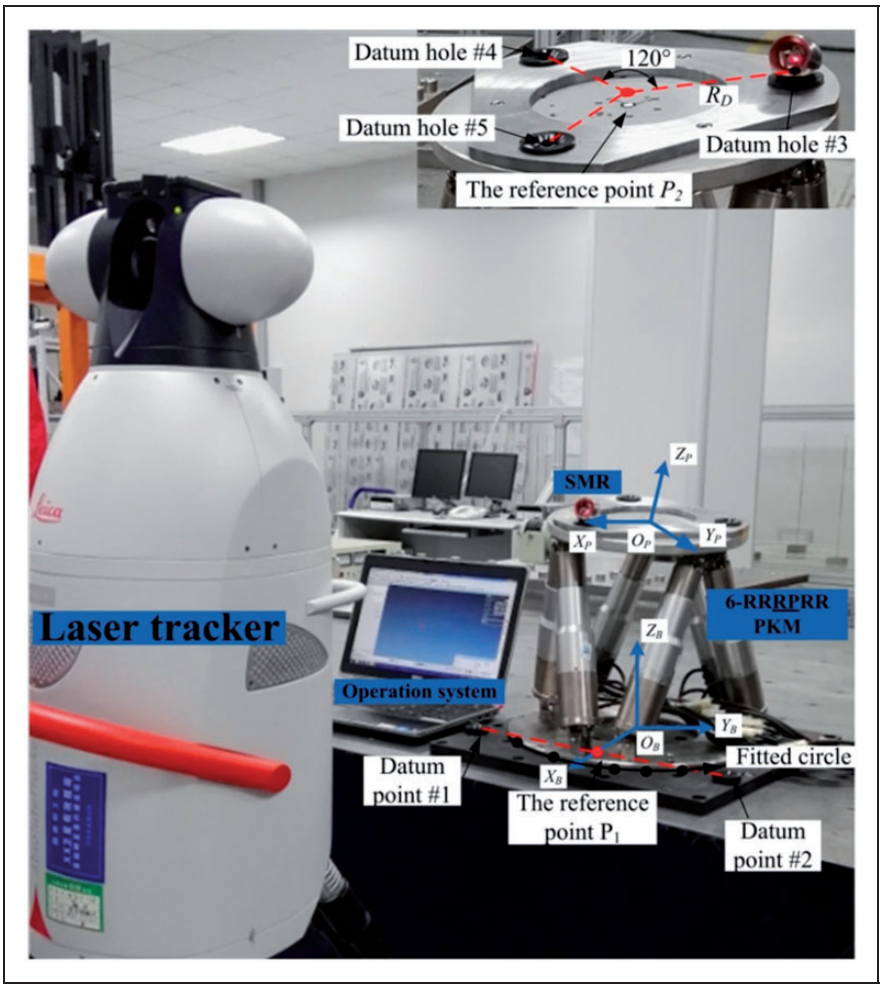

Figure 12. Configuration measurement experiments using a high-precision LT.

The pose measurement tool (as shown in Figure 12) processed three datum holes used to place reflector holder. Each datum hole was distributed at 120°, and R_D represents the distribution radius from the center point to the measurement points. Two datum points were symmetrically fixed to the plate tool. A removable reflector holder was placed along the edge of the base platform. The original point of O_P was defined at the center of the three SMRs; the Z_P axis was perpendicular to the plane which was formed by the centers of SMRs; and the X_P axis passes through the datum hole #5. The base coordinate system (O_B-$X_BY_BZ_B$) was set up as follows. Some measuring points were randomly selected to fit the upper surface of the lower platform, and the normal of this surface was the Z-axis. Several points were measured along the edge of the lower platform, as shown in Figure 12. A circle was fit with these points, and the center O_B of this circle was considered as the origin of system O_B-$X_BY_BZ_B$. The reference points P_1 was determined by the midpoint between datum point 1 and datum point 2; the X_B axis passed through the reference point P_1 and the origin O_B.

The measurement configuration from the moving coordinate system (O_P-$X_PY_PZ_P$) to base coordinate system (O_B-$X_BY_BZ_B$) was obtained by the PolyWorks software. In the kinematic calibration, the frame would have an offset along Z_B (or Z_P) axis to the geometric center of the base (or moving platform) based on the thickness of the base (or moving platform) and the reflector holders, and the radius of the SMR to make the identified parameters closer to their mathematical ones.

Structural parameter identification

The 29 measurement configuration results of the optimization selection procedure were used to identify the 54 structure parameters of the SMAM. The 29 groups of nominal limb variations were calculated using the inverse kinematic model, and the SMAM was driven by the controller. The actual 29 measurement configurations of the moving platform were obtained by the LT. The measurement procedure was as follows:

Step 1: Place the LT on the ground facing the auxiliary equipment, ensuring that the measurement distance is approximately 1.2 m, and the pitch angle is about zero.
Step 2: Automatically generate a measurement path and control code, and load the code into the SMAM control system.
Step 3: Power the LT controller and the tracking head, preheat the LT and calibrate it, and ensure the detection accuracy of LT.
Step 4: Move the SMR on datum hole #3 (as shown in Figure 12) without interrupting the laser path. Launch the control code and automatically collect the data along the measurement path, pausing the platform for 3 s at each nodal point for measurement. The 29 coordinate points are measured.
Step 5: Manually move the SMR to datum hole # 4, and repeat Step 4 to complete the measurement of the position data.
Step 6: Move the SMR to datum hole # 5, and repeat Step 4 to complete the measurement of the position data.

The calibration experiment of the SMAM was performed according to the above kinematic calibration process shown in Figure 3. The 54 identified structure parameter errors are listed in Table 5.

To validate the above calibration experiment, kinematics parameters that listed in Table 5 were updated in the controller system. The 29 optimal calibration poses with and without kinematic calibration are shown in Figure 13, the positioning accuracy of moving platform has been obviously improved. The experiment results show that the errors in the position and orientation vary substantially depending on the different calibration configurations.

The X-axis translation error is about 0.4 mm, and the Z-axis rotation error is about 0.1° before calibration. The positioning errors and the orientation errors are relatively homogeneous in different calibration poses after calibration. The maximum positioning error is reduced to about 0.01 mm, and the maximum orientation error is reduced to about 0.004° after calibration. The absolute accuracy of the SMAM is hence clearly improved.

Calibration experiment verification

To evaluate the global absolute accuracy of the SMAM, the workspace was divided into four sets through the plane $x = 0$ and $y = 0$, and there were 27 nodal points as measured points in $3 \times 3 \times 3$ magic box, measured path was planned form the start nodal point to the end nodal point, as illustrated in Figure 14. Eight random poses which involve rotation around the X-axis, Y-axis, and Z-axis needed to be detected at each nodal point, and the coordinate of datum holes #3, #4, and #5 would be measured at each pose by the LT. Therefore, a total of 216 poses and 972 ($27 \times 8 \times 3$) points needed to be measured.

The statistical results were presented in Table 6. The peak value of position error for 216 positions with and without calibration was 0.012 mm and 0.534 mm, respectively, and the corresponding standard deviations were 4.7e-3 mm and 0.076 mm, respectively. Similarly, the peak value of orientation error with and without calibration were 0.0051° and 0.122°, respectively, and the corresponding standard deviations with and without calibration were 0.0015° and 0.054°, respectively. As Figure 13 showed, the peak value errors with and without calibration occurred near the boundaries of the workspace. This phenomenon confirmed the necessity of optimal measurement configuration selection.

Table 5. Identified structure parameter errors (Unit:mm).

Numbers	Limb ΔL	Upper offset ΔL_P	Lower offset ΔL_B	Upper joint (ΔX_P ΔY_P ΔZ_P)	Lower joint (ΔX_B ΔY_B ΔZ_B)
I	−0.036	0.008	−0.017	−0.049	0.086
				0.017	−0.077
				−0.085	−0.089
II	0.079	−0.013	0.007	−0.108	0.051
				0.047	−0.048
				−0.124	0.030
III	0.042	0.014	−0.009	0.103	0.031
				0.012	0.049
				−0.124	0.027
IV	0.064	0.015	−0.019	0.039	−0.012
				0.063	−0.022
				−0.131	0.011
V	−0.070	−0.005	−0.017	−0.007	−0.015
				0.006	0.103
				−0.026	0.098
V	0.052	−0.013	0.009	0.038	0.059
				0.109	0.100
				−0.015	−0.066

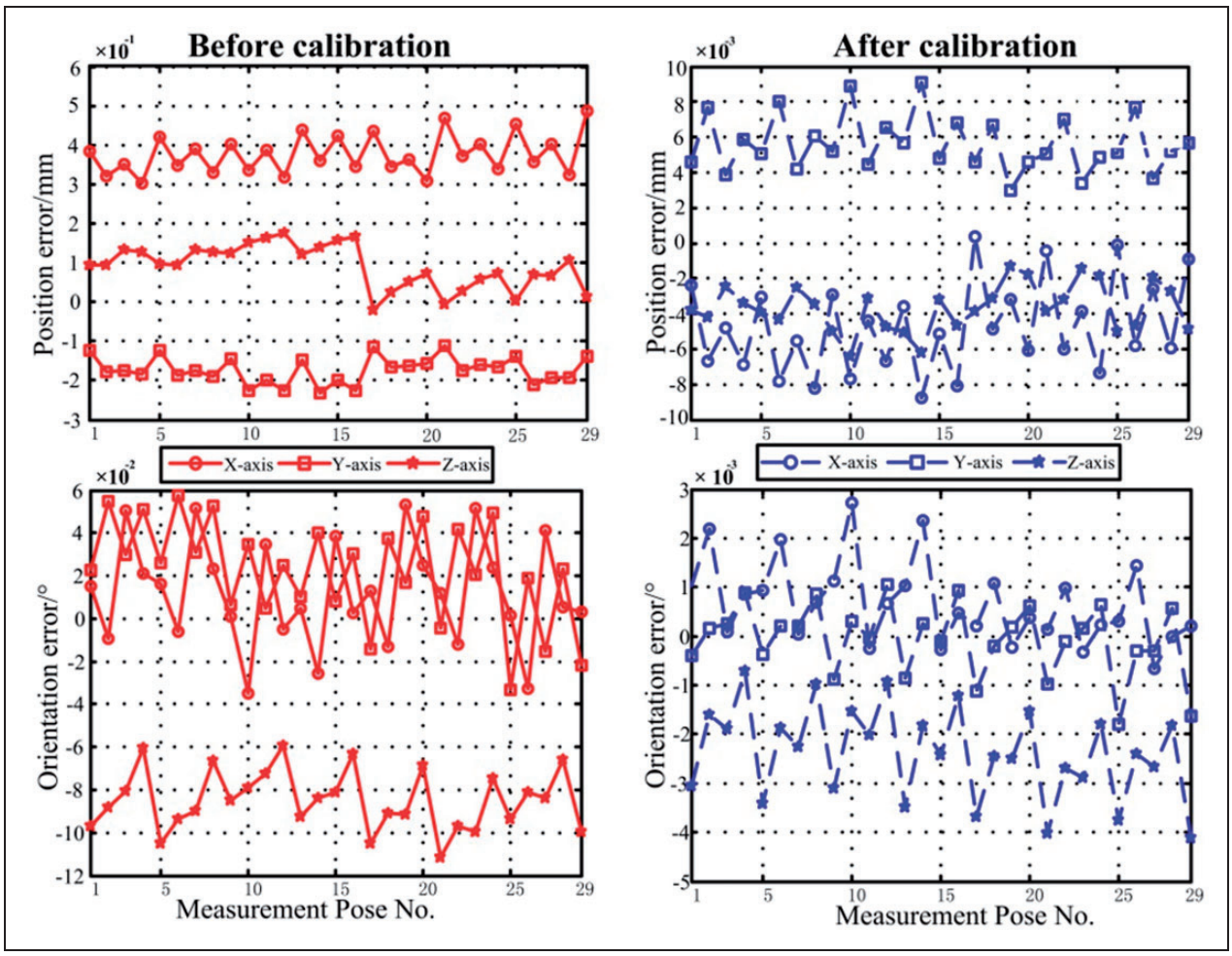

Figure 13. Error curves of 29 calibration poses.

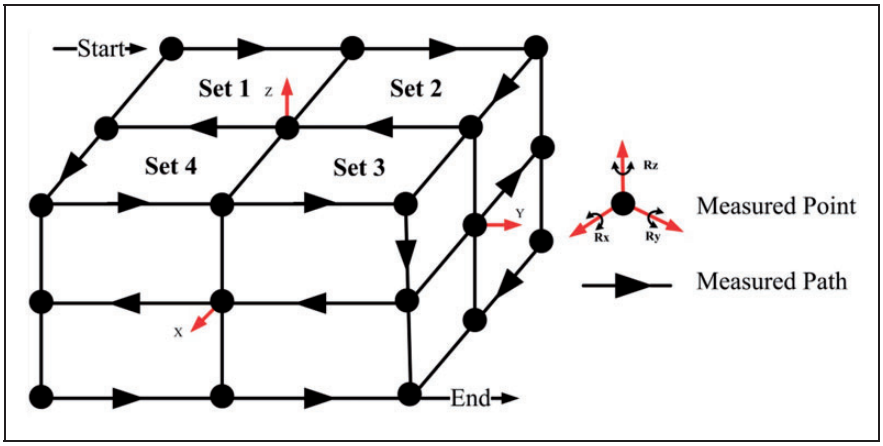

Figure 14. Measurement planning in the workspace for the experiment.

Table 6. Statistical results with and without calibration.

Error description / Calibration state	Position error (mm) Peak value	Position error (mm) Std dev	Orientation error (°) Peak value	Orientation error (°) Std dev
Before calibration	0.534	0.076	0.122	0.054
After calibration	1.2e-2	4.7e-3	5.1e-3	1.5e-3

Conclusions

In this paper, an accurate and efficient kinematic calibration based on the complete error model and optimal measurement configuration was proposed to improve the kinematic characteristics of the 6RRRPRR PKM. The conclusions were drawn as follows:

1. Considering the influence of RR-joint defects on the kinematic calibration precision, an error model including 54 structure parameter errors was derived. To verify the effectiveness of the complete error model, a comparison with non-complete error model was carried out by dealing with the calibration of the 6-RRRPRR parallel kinematic machine. An enormous improvement is achieved in the kinematic calibration when complete error model is employed.
2. In order to a compromise between calibration accuracy and efficiency, an optimal measurement configuration selection algorithm which included the optimal number and combinations of measurement configurations was proposed to determine the 29 optimal measurement configurations. A simulation was carried out to verify the efficiency and robustness of the calibration algorithm. Notably, using a few carefully chosen configurations is more effective for calibration than using many random configurations.
3. The kinematic calibration experiment based on a SMAM was carried out. The calibration results showed that maximum position error was reduced to 1.2e-2 mm, and the maximum orientation error was reduced to 0.0051°. The pose errors of the moving platform were substantially suppressed in the global workspace.
4. The experimental results showed that the proposed calibration method based on the complete error model and optimal measurement configuration was valid and effective, and can improve the pose accuracy of the 6-RRRPRR secondary-mirror positioning mechanism.

Declaration of Conflicting Interests

The author(s) declared no potential conflicts of interest with respect to the research, authorship, and/or publication of this article.

Funding

The author(s) disclosed receipt of the following financial support for the research, authorship, and/or publication of this article: This work was supported by the National Natural Science Foundation of China (Grant Number 11672290) and the Jilin Scientific and Technological Development Program (Grant Number 20160520074JH).

ORCID iD

Chunyang Han https://orcid.org/0000-0002-2509-1856

References

1. Sutherland W, Emerson J, Dalton G, et al. The visible and infrared survey telescope for astronomy (VISTA): design, technical overview, and performance. *Astron Astrophys* 2015; 575: A25.

2. Wildi FP, Brusa G, Riccardi A, et al. Toward first light of the 6.5-m MMT adaptive optics system with deformable secondary mirror. *Adapt Opt Syst Technol II: Int Soc Opt Photon* 2003; 4839: 155–164.
3. Lightsey PA, Atkinson CB, Clampin MC, et al. James Webb Space Telescope: large deployable cryogenic telescope in space. *Opt Eng* 2012; 51: 011003.
4. Yu Y, Xu Z-b, Wu Q-w, et al. Kinematic analysis and testing of a 6-RR RP RR parallel manipulator. *Proc IMechE, C: J Mechanical Engineering Science* 2017; 231: 2515–2527.
5. Lian B, Sun T, Song Y, et al. Stiffness analysis and experiment of a novel 5-DoF parallel kinematic machine considering gravitational effects. *Int J Mach Tools Manu* 2015; 95: 82–96.
6. Jiang Y, Li T and Wang L. Novel method for designing high precision parallel kinematic machines based on the smart structure. *IEEE/ASME Trans Mechatron* 2017; 22: 1889–1902.
7. Liu H, Huang T, Chetwynd DG, et al. Stiffness modeling of parallel mechanisms at limb and joint/link levels. *IEEE Trans Robot* 2017; 33: 734–741.
8. Mooring BW, Roth ZS and Driels MR. *Fundamentals of manipulator calibration*. Wiley: New York, 1991.
9. Han H, Han CY, Xu ZB, et al. Kinematics analysis and testing of novel 6-P-RR-R-RR parallel platform with offset RR-joints. *Proceedings of the Institution of Mechanical Engineers. Part C: Journal of Mechanical Engineering Science* 2019; 233: 3512–3530.
10. Gloess R and Lula B. Challenges of extreme load hexapod design and modularization for large ground-based telescopes. *Modern Technol Space- and Ground-based Teles Instrument: Int Soc Opt Photon* 2010; 7739: 77391U.
11. Karimi D and Nategh MJ. Kinematic nonlinearity analysis in hexapod machine tools: symmetry and regional accuracy of workspace. *Mech Mach Theory* 2014; 71: 115–125.
12. Cheng G, Yuan X, Yu J-l, et al. Kinematic calibration analysis of 3SPS + 1PS bionic parallel test platform for hip joint simulator. *Measurement* 2013; 46: 4152–4160.
13. Klimchik A, Furet B, Caro S, et al. Identification of the manipulator stiffness model parameters in industrial environment. *Mech Mach Theory* 2015; 90: 1–22.
14. Besnard S and Khalil W. Identifiable parameters for parallel robots kinematic calibration. In: *Proceedings 2001 ICRA IEEE international conference on robotics and automation (Cat No 01CH37164)*, IEEE, Seoul, South Korea, 21–26 May 2001, pp.2859–2866.
15. Li T, Li F, Jiang Y, et al. Kinematic calibration of a 3-P (Pa) S parallel-type spindle head considering the thermal error. *Mechatronics* 2017; 43: 86–98.
16. Tian W, Yin F, Liu H, et al. Kinematic calibration of a 3-DOF spindle head using a double ball bar. *Mech Mach Theory* 2016; 102: 167–178.
17. Jiang Y, Li T, Wang L, et al. Kinematic error modeling and identification of the over-constrained parallel kinematic machine. *Robot Comp-Integr Manu* 2018; 49: 105–119.
18. Pashkevich A, Chablat D and Wenger P. Kinematic calibration of Orthoglide-type mechanisms from observation of parallel leg motions. *Mechatronics* 2009; 19: 478–488.
19. Sun T, Zhai Y, Song Y, et al. Kinematic calibration of a 3-DoF rotational parallel manipulator using laser tracker. *Robot Comp-Integr Manu* 2016; 41: 78–91.
20. Kong L, Chen G, Zhang Z, et al. Kinematic calibration and investigation of the influence of universal joint errors on accuracy improvement for a 3-DOF parallel manipulator. *Robot Comp-Integr Manu* 2018; 49: 388–397.
21. Viegas C, Daney D, Tavakoli M, et al. Performance analysis and design of parallel kinematic machines using interval analysis. *Mech Mach Theory* 2017; 115: 218–236.
22. Wu Y, Klimchik A, Caro S, et al. Geometric calibration of industrial robots using enhanced partial pose measurements and design of experiments. *Robot Comp-Integr Manu* 2015; 35: 151–168.
23. Wu J-F, Zhang R, Wang R-H, et al. A systematic optimization approach for the calibration of parallel kinematics machine tools by a laser tracker. *Int J Mach Tools Manu* 2014; 86: 1–11.
24. Schröer K, Albright SL and Grethlein M. Complete, minimal and model-continuous kinematic models for robot calibration. *Robot Comp-Integr Manu* 1997; 13: 73–85.
25. Zhou W, Chen W, Liu H, et al. A new forward kinematic algorithm for a general Stewart platform. *Mech Mach Theory* 2015; 87: 177–190.
26. Chiu Y-J and Perng M-H. Self-calibration of a general hexapod manipulator using cylinder constraints. *Int J Mach Tools Manu* 2003; 43: 1051–1066.
27. Ren X-D, Feng Z-R and Su C-P. A new calibration method for parallel kinematics machine tools using orientation constraint. *Int J Mach Tools Manu* 2009; 49: 708–721.
28. Jeon D, Kim K, Jeong J, et al. A calibration method of redundantly actuated parallel mechanism machines based on projection technique. *CIRP Ann* 2010; 59: 413–416.
29. Khalil W and Dombre E. *Modeling, identification and control of robots*. Oxford, UK: Butterworth-Heinemann, 2004.
30. Huang T, Chetwynd DG, Whitehouse DJ, et al. A general and novel approach for parameter identification of 6-DOF parallel kinematic machines. *Mech Mach Theory* 2005; 40: 219–239.
31. Song Y, Zhang J, Lian B, et al. Kinematic calibration of a 5-DoF parallel kinematic machine. *Precis Eng* 2016; 45: 242–261.
32. Hoevenaars A, Gosselin C, Lambert P, et al. A systematic approach for the Jacobian analysis of parallel manipulators with two end-effectors. *Mech Mach Theory* 2017; 109: 171–194.
33. Sun T and Lian B. Stiffness and mass optimization of parallel kinematic machine. *Mech Mach Theory* 2018; 120: 73–88.
34. Carrillo H, Birbach O, Täubig H, et al. On task-oriented criteria for configurations selection in robot calibration. In: *IEEE International Conference on Robotics and Automation*, Karlsruhe, Germany, 6–10 May 2013, pp.3653–3659.
35. Daney D, Papegay Y and Madeline B. Choosing measurement poses for robot calibration with the local convergence method and Tabu search. *Int J Robot Res* 2005; 24: 501–518.

36. Zhou J, Nguyen H-N and Kang H-J. Selecting optimal measurement poses for kinematic calibration of industrial robots. *Adv Mech Eng* 2014; 6: 291389.
37. Nategh M and Agheli M. A total solution to kinematic calibration of hexapod machine tools with a minimum number of measurement configurations and superior accuracies. *Int J Mach Tools Manu* 2009; 49: 1155–1164.
38. Jia Q, Wang S, Chen G, et al. A novel optimal design of measurement configurations in robot calibration. *Math Probl Eng* 2018; 2018.
39. Merlet J-P. Jacobian, manipulability, condition number, and accuracy of parallel robots. *J Mech Des* 2006; 128: 199–206.
40. Nahvi A and Hollerbach JM. The noise amplification index for optimal pose selection in robot calibration. In: *Proceedings of IEEE international conference on robotics and automation*. Piscataway, NJ: IEEE, 1996, pp.647–654.
41. Driels MR and Pathre US. Significance of observation strategy on the design of robot calibration experiments. *J Robot Syst* 1990; 7: 197–223.
42. Khalil W, Gautier M and Enguehard C. Identifiable parameters and optimum configurations for robots calibration. *Robotica* 1991; 9: 63–70.